Wind and Structures, Vol. 15, No. 6 (2012) 509-529
DOI: http://dx.doi.org/10.12989/was.2012.15.6.509

Pressure field of a rotating square plate with application to windborne debris

P. Martinez-Vazquez*[1], B. Kakimpa[2], M. Sterling[1], C.J. Baker[1], A.D. Quinn[1],
P.J. Richards[3] and J.S. Owen[2]

[1]*School of Civil Engineering, University of Birmingham, UK*
[2]*Department of Civil Engineering, University of Nottingham, UK*
[3]*Department of Mechanical Engineering, University of Auckland, New Zealand*

(Received January 27, 2011, Revised February 1, 2012, Accepted February 2, 2012)

Abstract. Traditionally, a quasi steady response concerning the aerodynamic force and moment coefficients acting on a flat plate while 'flying' through the air has been assumed. Such an assumption has enabled the flight paths of windborne debris to be predicted and an indication of its potential damage to be inferred. In order to investigate this assumption in detail, a series of physical and numerical simulations relating to flat plates subject to autorotation has been undertaken. The physical experiments have been carried out using a novel pressure acquisition technique which provides a description of the pressure distribution on a square plate which was allowed to auto-rotate at different speeds by modifying the velocity of the incoming flow. The current work has for the first time, enabled characteristic pressure signals on the surface of an auto-rotating flat plate to be attributed to vortex shedding.

Keywords: auto-rotation; surface pressures; coherent structures; vortex shedding

1. Introduction

The wind engineering community is coming to realise that the impact loading due to windborne debris can be of some significance (Holmes 2004). In practical terms the requirement is for the specification of debris speed (or energy) as a function of debris type and distance of the structure from potential debris sources. In recent years wind tunnel measurements of debris flight have been carried out by Wang and Letchford (2003), Holmes (2004) and Holmes *et al.* (2004). These experiments included the measurement of debris trajectories and velocities and some comparisons were made with the results of calculations using the debris flight equations. A significant conclusion implicit in all these investigations was that, to a large extent, the behaviour of compact and sheet debris can be taken to be approximately two dimensional, with translations and rotations occurring mainly in the vertical plane in the direction of the mean wind field.

Baker (2007) has presented a thorough analysis of the two-dimensional debris flight equations. For sheet debris the situation is more complex and drag and lift force coefficients and pitching moment coefficients also need to be specified, both as a function of the inclination of the sheet to the flow, and as a function of the rotational velocity. Tachikawa (1983) showed that, for the sheet at

---

* Corresponding author, Dr., E-mail: p.vazquez@bham.ac.uk

an instantaneous angle to the relative flow direction, these coefficients can be regarded as the sum of the quasi-static coefficients (those measured at a fixed inclination to the flow) and the auto-rotation coefficients, due to streamline displacement (i.e., the "Magnus" effect). On the basis of the small amount of experimental data that existed at the time, Baker assumed that the side and lift force and pitching moment coefficients followed a quasi-steady response.

Richards *et al.* (2008) adopted a different approach to Baker and by using simple wing theory was able to derive a model capable of predicting the mean 3-dimensional motion of plate type debris. Richards *et al.* also obtained an extensive series of force and moment coefficient data relating to plate debris of selected aspect ratios at a wide range of orientations to the oncoming flow within the University of Auckland's twisted flow wind tunnel. These data were obtained under static conditions, i.e., the plates were not allowed to move within the flow and as such it is questionable how representative these values were compared to those experienced by plates as they fly through the air. Hence, it was considered appropriate to investigate the aerodynamics of plates during free flight but also during auto-rotation; it is with the latter that the current work is concerned.

Auto-rotation is a phenomenon of relevance to a variety of different engineering fields and has been discussed in the past by a number of authors - see for example Riabouchinsky (1935). For auto-rotating plates, Lugt (1983) identified different forms of autorotation undertaken by windmills and propellers (axis of rotation parallel to the flow) and airfoils, wings, and flaps (axis of rotation perpendicular to the flow). The aerodynamics of these elements was studied further by Newmark (1963), Daniels (1970) and Cohen (1976), whilst the particular case of plates that resemble common shapes driven by strong winds was studied analytically and experimentally by Dupleich (1941), Bustamante and Stone (1969), Smith (1971), Glaser and Northup (1971), Iversen (1979), Tachikawa (1983), and Lugt (1983) amongst others. These contributions have helped to better understand the complex mechanisms related to auto-rotation and have provided several approaches for calculating the tip velocity for plates of different shapes. The aforementioned work has influenced other researchers who have undertaken further experimental and analytical investigations for studying aerodynamic effects on fixed-axis and free flying rotating elements, see for example, Wang and Letchford (2003), Holmes *et al.* (2006), Baker (2007), Richards *et al.* (2008), Martinez-Vazquez et *al*. (2009, 2010) and Kordi *et al.* (2010). In addition, computational models for studying the aerodynamics of auto-rotating elements have emerged given the challenge imposed by the complex non-linear fluid-structure interaction – see for example Lugt (1980), Mittal *et al.* (2004) and Andronov *et al.* (2007). These studies have however been exclusively concerned with two-dimensional auto-rotation of high-aspect-ratio plates whose wake topology and flow structure has been found to be qualitatively different from that exhibited by low-aspect-ratio plates mainly due to the presence of strong tip vortices that interact with the leading edge vortex (see for example Taira *et al.* 2009). Computational models of low aspect ratio plate rotation such as Dong *et al*. (2006) have previously been presented however these deal with prescribed motions such as those involved during insect flight (Wang 2005) rather than with free autorotation where plate motion is determined by the non-linear fluid-structure interaction. Thus, in order to address these limitations, some new approaches have been developed in the recent years by Kakimpa *et al.* (2010a,b). In Kakimpa *et al.* (2010a), an unsteady computational fluid dynamics (CFD) model is used to simulate the unsteady non-uniform flow field around a rotating plate similar to that used in the experimental work reported by Martinez-Vazquez *et al.* (2010). In order to simulate plate motion, the CFD model is coupled sequentially with a rigid body dynamics (RBD) (see Kakimpa *et al.* 2010b,c) that is globally singularity free for all possible orientations in three dimensions. This coupled CFD-RBD approach allows for a more complete simulation of the non-linear FSI involved in autorotation of flat elements as well as the inclusion of a wider variety of shapes.

In the current work, the aforementioned CFD-RBD model has been validated against the physical measurements undertaken by Martinez-Vazquez *et al.* (2010) and subsequently used to obtain information on the nature of the wake flow field during auto-rotation. The present investigation extends the previous work and has two main objectives: firstly, to describe the experimentally determined pressure field of an auto-rotating square plate, and secondly, to examine the relationship between the unsteady disturbances outlined in the measured data above and simulated flow field.

The paper is organised as follows: section 2 describes the experimental set up, while Section 3 describes how the corresponding auto-rotational periods and average force coefficients were estimated by Martinez-Vazquez *et al.* (2010). Section 4 examines the same experimental data in non-averaged form in order to examine particular features present in some of the data, and in section 5, coherent structures observed in the non-average pressure field are hypothesised. Section 6 introduces the CFD model in order to corroborate the existence of such coherent structures in a three-dimensional computational environment, while Section 7 suggests a link between coherent structures observed on the plate with vortex shedding observed in the flow field. Finally, appropriate conclusions are drawn in Section 8.

2. Experimental setting

In the work outlined below, a test-sheet, representing a typical roof cladding panel, was made of polystyrene. The test-sheet was 1 m square, had a thickness of 0.025 m and weighed 2.7 kg. Embedded within the test-sheet were 24 pressure sensors, 7 data loggers and 1 gyroscope. The differential pressure transducers were manufactured by Sensortechnics and had an output voltage and pressure acceptance in the range of 0.25-4.5 V and 0-2.5 mbar, respectively. The gyroscope was part of an analogue inertial measurement unit (*AccelRate3D*) manufactured by Omni instruments. The maximum acceleration capacity and rate of rotation of the gyroscope was 10 g and 600^{o}/sec respectively. The unit required a 5 V direct current supply for operation. For the data logger, a portable card *XR440-M* manufactured by Omni instruments was considered suitable to work in combination with the sensors and gyroscope. One data logger was capable of interfacing with up to 4 pressure sensors or one gyroscope. Each data logger accepted input signals of 0-5 V, in addition to providing a resolution of 12 bits with a maximum sampling frequency of 200 Hz and a timing accuracy of 0.5 %. In the data loggers a 9 V battery is used which is also sufficient to power the pressure sensors and gyroscope. The general characteristics of the experimental test-sheets are shown in Fig. 1(a).

The supporting system for the test-sheet (Fig. 1(b)) consisted of two metallic frames of height 1.5 m. Each support had a vertical plate at the top extreme where an aluminium frame which was attached to the polystyrene test-sheet could be inserted using a pin connector. During the tests, rotation around the z axis was permitted whilst any other degree of freedom remained restricted. The angle formed between the plate and the horizontal plane, is defined as the pitch angle. The experiments were carried out in the Twisted Flow Wind Tunnel at the University of Auckland in New Zealand, using uniform wind speeds of U = 5, 7.5 and 10 m/s and turbulence intensities within the range of 2% - 3% at 1.5 m above the ground. The duration of each experiment was of ~120 s and the data was recorded at 200 Hz. Further details about the experiment can be found in Martinez-Vazquez *et al.* (2009, 2010).

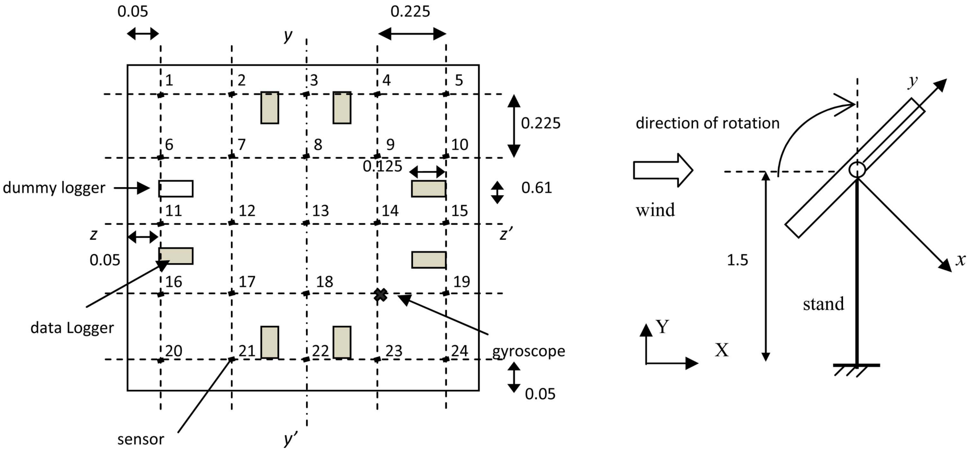

(a) Test-sheet (front view) (b) Test-sheet on bearings (lateral view)

Fig. 1 (a) Logging system configuration and (b) bearing plus reference system - (distances in m)

3. Auto-rotational periods

As outlined previously, the experimental data used for the present investigation has been discussed in ensemble averaged form in Martinez-Vazquez *et al.* (2010), where a parametric analysis was undertaken and relevant aerodynamic effects were discussed. In that work, the test-sheet was released at a pitch angle $\alpha \sim 15^{\circ}$ from its horizontal position, passing the transition stage (the interval between the position of release and stable auto-rotation) within approximately 30 s. Every auto-rotational test lasted about 107 seconds, i.e., 30 s for the initial start of the wind tunnel plus 77 s which covered the auto-rotational event. Only the last 30 seconds were considered for analysis in order to guarantee that the flow was fully developed and the board was under stable autorotation. Fig. 2 shows a typical five-second time window which illustrates the variation of the normal pressure coefficient defined as $C_{NP} = P / 0.5\rho U^2$ (where P represents net pressure across the test-sheet and ρ is the air density) during a typical run. In this figure, the variation of C_{NP} with respect to time is illustrated for four sensors located at the corners, i.e., #1, #5, #20, and #24 and sensor #13 which was located at the centre of the board (c.f. Fig. 1).

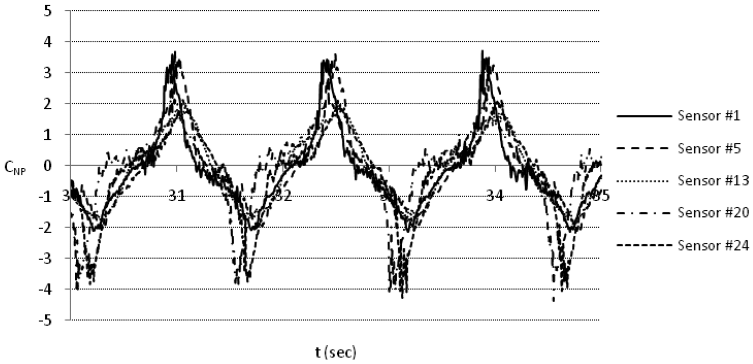

Fig. 2 Five-second series of net pressure coefficients at four sensors on the board, U = 7.5 m/s

Computation of the normal force coefficients defined as $C_N = F / 0.5\rho U^2 A$ – where F and A represent the total force induced by the surface pressures and area of the plate respectively, was achieved through an integration of the net pressure coefficients over A. The force coefficients were then observed on an ensemble-averaged characteristic cycle from where the following average rotation periods were inferred: 2.06 s, 1.36 s, and 1.11 s, for wind velocities of $U = 5$, 7.5, and 10 m/s, respectively (Martinez-Vazquez *et al.* 2010). The rotational frequency (n_0) for each case is 0.485 Hz, 0.735 Hz, and 0.90 Hz. The corresponding Strouhal number (defined as $St = n_0 L / U$ - where L represent the chord length of the test-sheet) are 0.097, 0.098, and 0.09, whilst the Reynolds number, ($R_e = \rho UL / \mu_{air}$ – where μ represents the dynamic viscosity of air) ranged between $3.4 \times 10^6 - 6.8 \times 10^6$.

4. Non-averaged pressures

A detailed description of the cyclical variation of the pressure field can be observed in Fig. 3, where the experimentally determined C_{NP} per sensor / per cycle is shown. In these plots, the value of C_{NP} is represented (along the vertical axis) for a set of angles covering half-cycle at intervals of 30° measured from the horizontal position of the test-sheet, i.e., $\alpha = 0^\circ$ for $U = 7.5$ m/s (similar patterns are observed for $U = 5$, 10 m/s but for the purposes of brevity are not illustrated). Note that there are 24 sensors and 18 cycles represented in each case and that those values of $C_{NP} < 2.5$ are represented by dark colours. The cyclical variation of C_{NP} observed in this figure has been evaluated

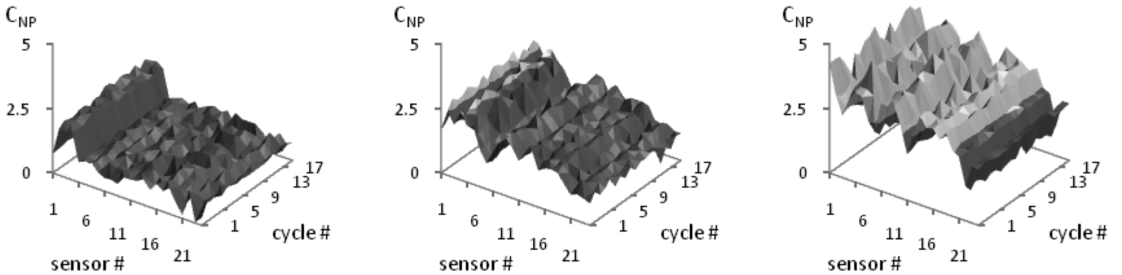

(a) $\alpha = 30^\circ$ (b) $\alpha = 60^\circ$ (c) $\alpha = 90^\circ$

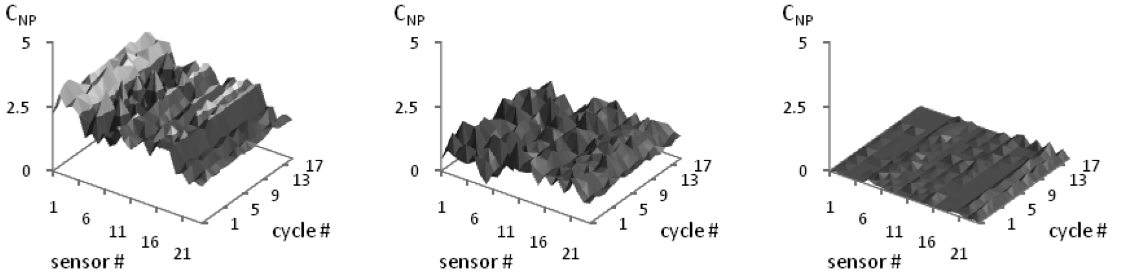

(d) $\alpha = 120^\circ$ (e) $\alpha = 150^\circ$ (f) $\alpha = 180^\circ$

Fig. 3 C_{NP} experimentally determined per sensor / per cycle at different angular positions of the test-sheet, for $U = 7.5$ m/s in previous work (Martinez-Vazquez *et al.* 2009) where the same experimental setting as the one reported here was used to measure autorotational forces. In that investigation, the variation of subsequent peaks was interpreted in terms of the index $I_v = \frac{\sigma}{\mu}$ (where μ and σ represent the mean and standard deviation of the total area under the pressure peaks shown in Fig. 2). The value of I_v estimated in the aforementioned work did not exceed 2% which suggested that the general features observed in each cycle were similar.

It can be observed in Fig. 3, that during the half-cycle the normal force is mainly concentrated at the leading edge, i.e., the top of the test-sheet (sensors #1 to #5). It is also worth noting that at $\alpha = 90^\circ$ the pressure distribution is not uniform but rather more asymmetric than the one observed at $\alpha = 30^\circ$ and 60°. At angles around 150°, the pressure distribution is such that the net torque tends to act in order to stop the rotational motion (retarding torque as defined by Lugt 1983), however the level of pressures does not reach those observed at $\alpha = 90^\circ$, whilst their lower limit is observed at pitch angles of around 180°. The asymmetric pressure distribution described above, results in a net torque after each half-cycle, which ultimately appears to induce stable auto-rotation.

In Fig. 4, the normal force coefficients (C_{NP}) have been represented over the surface of the test sheet. The data corresponds to one cycle only (cycle 17) and is shown for the set of angles presented in Fig. 3. The coordinates (y, z) in Fig. 4, define the surface of the test-sheet which is bounded by the location of the pressure sensors, i.e., $-0.45 \leq y \leq 0.45$ and $-0.45 < z < 0.45$ (see Fig. 1) – where ($y = 0$, $z = 0$) defines the geometrical centre of the test-sheet. The values associated with each contour correspond to the magnitude of C_{NP} which for the regions between pressure sensors were determined by using cubic interpolation.

Fig. 4 shows more explicitly the pressure distribution shown in Fig. 3. The high pressure observed

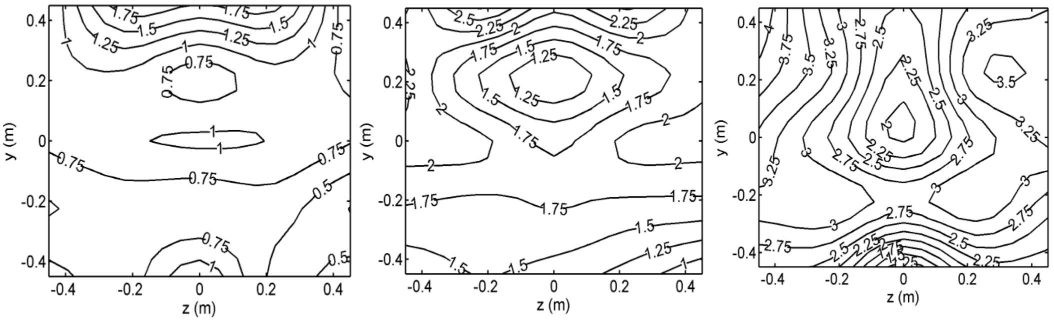

(a) $\alpha = 30^\circ$ (b) $\alpha = 60^\circ$ (c) $\alpha = 90^\circ$

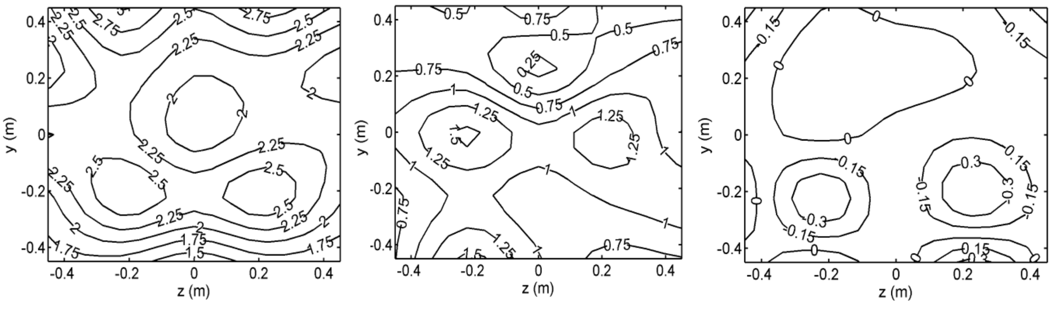

(d) $\alpha = 120^\circ$ (e) $\alpha = 150^\circ$ (f) $\alpha = 180^\circ$

Fig. 4 C_{NP} corresponding to one cycle (cycle 17) represented over the test-sheet, for $U = 7.5$ m/s at the leading edge for $\alpha = 30°$ is rather concentrated over its central region with a relatively smooth transition towards the bottom edge where values within the interval 0 - 1 are observed. A relatively similar pressure distribution is observed for α = 60° but with larger magnitudes of C_{NP} for example at the sides of the test-sheet. The high concentration of pressures at the sides becomes more clear for $\alpha = 90°$ where pressure peaks in the interval $3 < C_{NP} < 4$, dominate. At $\alpha = 90°$, there also appears a region of low pressure at the bottom edge, which is more pronounced around the centre. The pressure configuration at α = 60° and α = 90° is not unlike that observed at α = 120° although in the second case the higher pressures at the sides diminish and the peaks appear to concentrate along the upper and bottom edges. At α = 150° the values of C_{NP} decay all over the surface tending to values approaching to zero at α = 180°, when the test-sheet reached the horizontal position after half-cycle.

5. Rate of change

The experimental data discussed above was examined further cycle by cycle for each sensor. The non-averaged data revealed the existence of local disturbances which appeared at different angular interval depending on the location of the sensor on the test-sheet. Figs. 5 and 6, show examples of

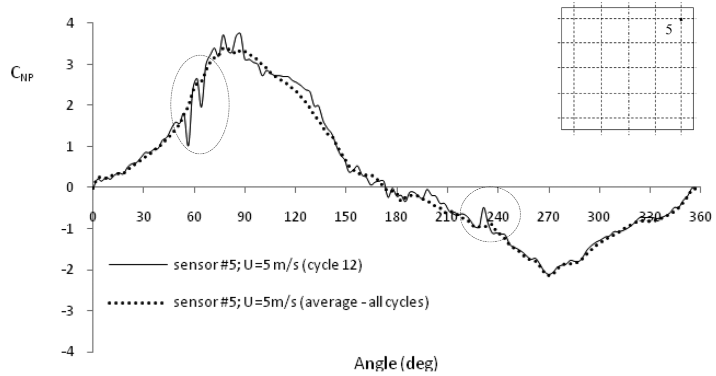

Fig. 5 Pressure disturbances registered by sensor # 5, for U = 5 m/s

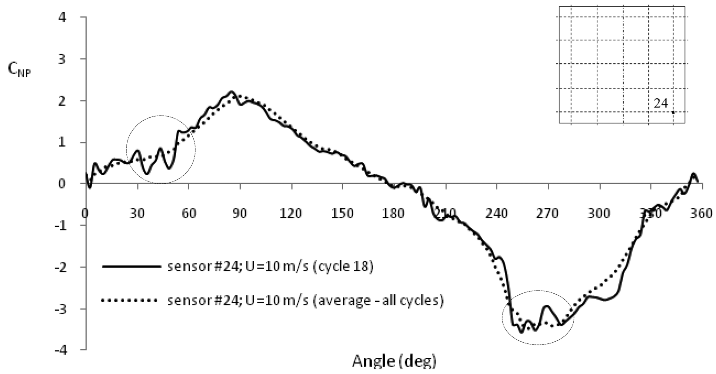

Fig. 6 Pressure disturbances registered by sensor # 24, for U = 10 m/s

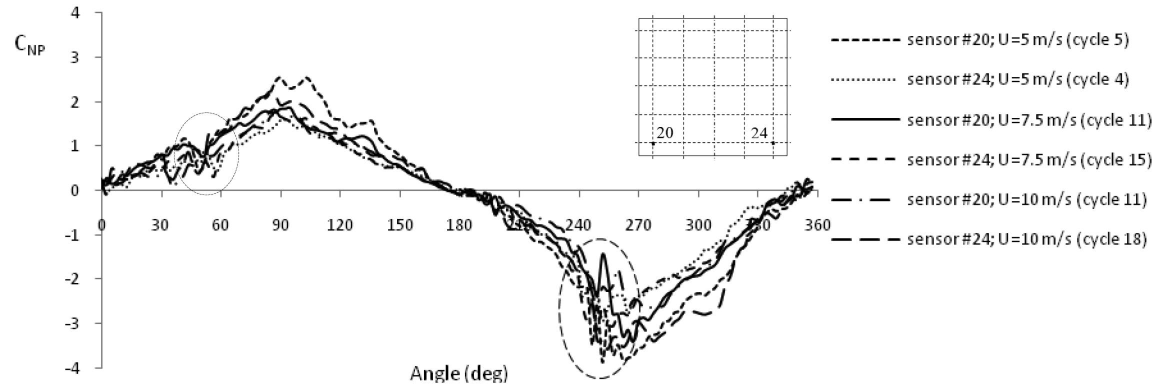

Fig. 7 Pressure disturbances registered by sensor #20 and #24, for U = 5 m/s, 7.5 m/s, and 10 m/s

this for the data recorded by sensors #5 and #24, for wind velocities of U = 5 m/s and 10 m/s, respectively. In these figures, the average force coefficients estimated by using all cycles registered with each sensor have been included for comparison.

Fig. 7 illustrates that the angular interval in which the local disturbances appear do not vary with the velocity of the incoming flow. In Fig. 7, data relating to sensors located at bottom (corners) is shown for U = 5, 7.5, and 10 m/s.

The highlighted regions in Fig. 7 correspond to angular intervals of 30° - 60° and 240° - 270°, i.e., at an angle of ca. 60° from the start of each half cycle. It can be observed that the characteristic signatures do not occur at specific angles but rather within certain angular intervals suggesting that whatever flow feature is causing these disturbances is unsteady.

As discussed above, the ensemble-average data from all sensors tends to eliminate the unsteady pressure fluctuations. Thus, in order to evaluate the local disturbances shown in Fig. 7, the rate of change (R) of the series of fluctuating normal force coefficients, converted to zero-mean processes, were examined on a cycle by cycle basis as described below.

The value of R was obtained by using samples of data formed by a number of points covering between 7 - 15° within a cycle, i.e., more than one iteration was made. Each sample was separated by one data point (p), for example, $s_i = \{p_i, p_{i+1} \ldots, p_{i+Q}\}$; $s_{i+1} = \{ p_{i+1} \ldots, p_{i+1+Q}\}$; *etc.*, where s_i, s_{i+1}, are consecutive samples and $Q+1$ is the number of points included. A straight line was then fitted to each series so that its slope was associated to middle point on each case. In this study, a value of $Q = 3$ was finally used, although for the sake of generality, all equations are presented here in terms of the variable Q.

In Eq. (1), R_α denotes the rate of change of the pressure fluctuations with respect to the rotational angle (α), and $\hat{C}_{NP}$ is the average zero-mean pressure coefficient estimated for each data sample defined above. The domain of the pressure fluctuations (Ψ) can thus be defined as formed by the surface of the rotating test-sheet, which is bounded by the linear and angular coordinates -0.45 m $\leq y \leq +0.45$ m; -0.45 m $\leq z \leq +0.45$ m; $0 \leq \alpha < 360°$. The upper and lower limit of (y, z) is given by the largest distance of any sensor with respect to the geometric centre of the test-sheet in a Cartesian reference system. The general form of R, namely, the rate of change of pressure fluctuations projected onto Ψ, is thus given by Eq. (2) below.

$$R_\alpha = \frac{\partial \hat{C}_{NP}}{\partial \alpha} \tag{1}$$

$$R_{y,z,\alpha} = \frac{\partial \hat{C}_{NP}}{\partial y} + \frac{\partial \hat{C}_{NP}}{\partial z} + \frac{\partial \hat{C}_{NP}}{\partial \alpha} \tag{2}$$

In physical terms, R_α describes how quick the disturbed pressures change (for example by taking as a reference the local mean) when one moves in the direction of α. This enables the extension (within Ψ) of the characteristic signatures shown in Figs. 5 -7 to be determined.

In addition, the cross correlation of the data samples defined above, amongst all sensors (centred at an angle α) was calculated. This correlation is defined in Eq. (3) - where E^Q *[.]*, σ_w^Q represent the expected value and *rms* of the group of $Q+1$ data points $p_{w,i}$, respectively. In this case, w identifies the sensor, i.e., $w = \{1 \ldots W = 24\}$ whilst $p_{w,q}$ is the *q-th* point in the data sample $s_{wi} = \{p_{w,i}, p_{w,i+1} \ldots, p_{w,i+Q}\}$. In Eq. (3), the subscript α identifies the angle within the range $0 < \alpha \leq 360^\circ$ at which the corresponding data sample is centred, whilst j, k identify the sensors for which $C_{jk\text{-}\alpha}$ is being estimated.

$$C_{jk,\,\alpha} = \frac{1}{Q+1}\left[\frac{\sum_q (p_{jq} - E^Q[\alpha_j])(p_{kq} - E^Q[\alpha_k])}{\sigma_j^Q \sigma_k^Q}\right]_\alpha \tag{3}$$

The definitions given by Eqs. (1)-(3) have been used in order to infer the existence of coherent structures in the domain (Ψ). Thus, we have assumed that a coherent structure would be characterised by a region in Ψ where correlated peak values of R occur. In the current work, a coherent structure is simply defined as a region of organised ‘fluctuations’ (characteristic signatures) that are distinct from the average variations and occur solely in the pressure field on the flat-plate. To avoid confusion, regions of repeating patterns which occur in the flow field are termed vortex structures or vortex shedding (see Section 7).

As observed in Fig. 7, pressure fluctuations occur at different angles on each cycle. Thus, the peak values obtained by using Eq. (1) fall into different values of α within Ψ. This is illustrated in Figs. 8-10, for sensors #5 (upper right corner), #13 (centre), and #20 (lower left corner). Note that since these results were estimated by using zero-mean processes, the average value of R_α over all cycles equals the rate of change of the average series, i.e., zero.

It can be seen in these figures that the peak values of R_α are concentrated in specific angular intervals. These are for example $60^\circ \leq \alpha < 90^\circ$ and $240^\circ \leq \alpha < 270^\circ$, for sensors #5 and #20, respectively. The results shown in Figs. 8-10 suggest that, coherent structures in the domain Ψ

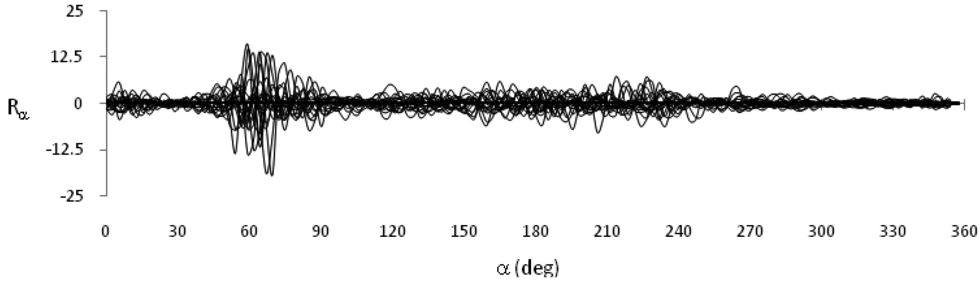

Fig. 8 Parameter R_α estimated for all cycles registered at sensor #5, for $U = 7.5$ m/s

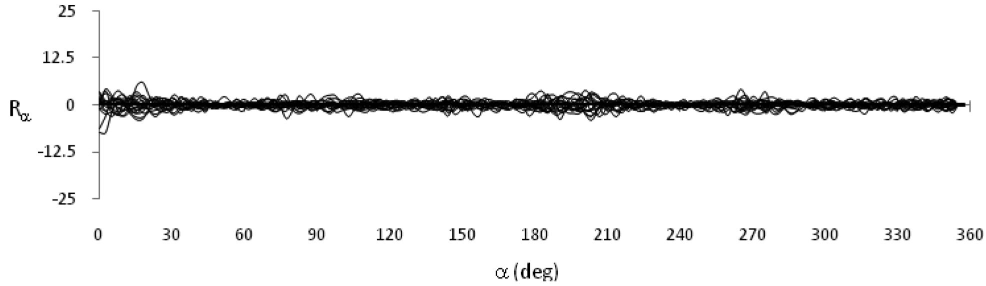

Fig. 9 Parameter R_α estimated for all cycles registered at sensor #13 for U = 7.5 m/s

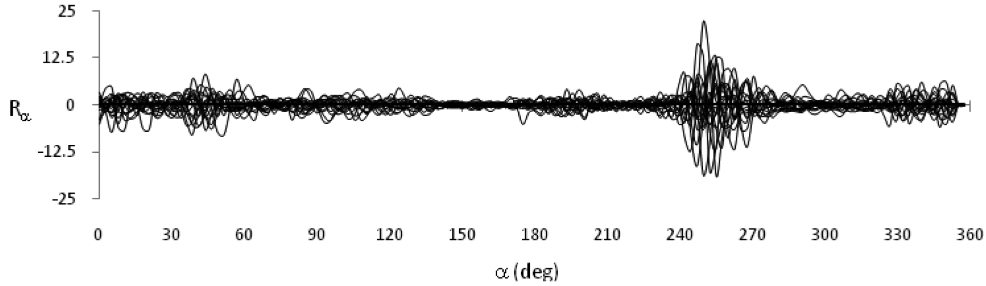

Fig. 10 Parameter R_α estimated for all cycles registered at sensor #20 for U = 7.5 m/s

would be observed at different angles on each cycle and that such structures are more likely to be observed at the periphery of the test-sheet than at its geometrical centre – see Fig. 9. Moreover, according to Eq. (2), such structures would be identifiable by plotting the estimated value of R_α on the plane (y, z), defined by the coordinates of each sensor on the test-sheet, i.e., from these plots the value of $R_{y,z,\alpha}$ can be inferred. This is presented in Figs. 11 and 12 for a series of combinations *(k, α)*, where k is the *k-th* cycle registered during the autorotational tests for U = 7.5 m/s and α is the angle where the peak R_α was observed. In these figures, the correlation parameter shown corresponds to one of the sensors located in the region of peak values of R_α.

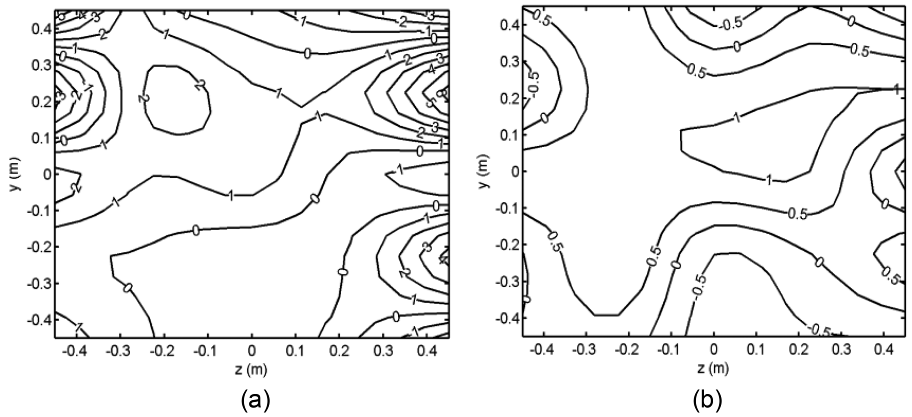

(a) (b)

Fig. 11 (a) Value of R_α estimated at α = 84° during cycle 15 and (b) correlation parameter defined for sensor #10, for U = 7.5 m/s

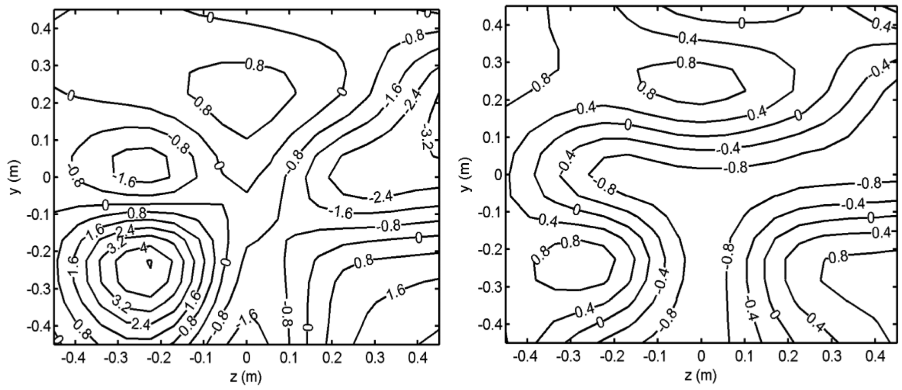

(a) (b)

Fig. 12 (a) Value of R_α estimated at α = 270° during cycle 10, and (b) correlation parameter defined for sensor #17, for U = 7.5 m/s

Figs. 11 and 12 illustrate regions where peak values of R_α are combined with local high correlation. Fig. 11(a) which corresponds to α = 84° (cycle 15) shows peak pressures which concentrate at the corners and are more clearly at the upper sides. Fig. 11(b) shows that the sensor # 10 appears to be highly correlated with sensors located around it but also with those distributed over the upper left quadrant where high values of R_α are also observed in Fig. 11(a). Fig. 12(a) presents similar patterns. In this case, peak values of R_α are observed at the lower corners from where a coherent structure would be identified at the left hand side. The cross correlation in Fig. 12(b) corresponds to sensor #17 which falls within this region of peak R_α's – see locations in Fig. 1. From this figure, it can be seen that although there is a local correlation around sensor #17, its high correlation with sensors located at the right corner suggest that the pressure disturbances described by R_α would be occurring at similar rates at both corners.

Figs. 11 and 12 show examples of peak values of R_α that are accompanied by high local correlation. However, as stated above in this section, such combination occurs at different angles on each cycle, apparently due to the unsteadiness of this phenomenon. A general view of the different regions where the coherent structures (as defined by Eqs. (1)-(3)) are located during the autorotational event can be given by averaging the absolute value of R_α registered in all cycles for all sensors. These results, are shown in Fig. 13, for the angular regions centred at α = 60°, 90°, 240°, 270°, which are the angular positions within a cycle where the highest disturbances given by R_α have been observed during the autorotation of the test-sheet.

In Fig. 13 the regions where coherent structures have been identified become more evident. These are consistent with regions of high disturbance shown in Figs. 8-10 as well as with the areas in which coherent structures corresponding to one cycle only have been observed, as illustrated in Figs. 11 and 12. Note that since these structures have been defined as to be contained within the domain Ψ, they refer directly to the pressure field.

It is perhaps worth reflecting that the experimental data outlined above does not provide direct evidence of the relationship between the pressure and the flow field. In addition, although coherent structures (as defined above) have been identified on the test-sheet, the "traditional" view of coherent structures tends to conjure images of organised eddies within the flow. Hence, to ascertain if patterns observed above do indeed result in a 'traditional' type of coherent structure, information

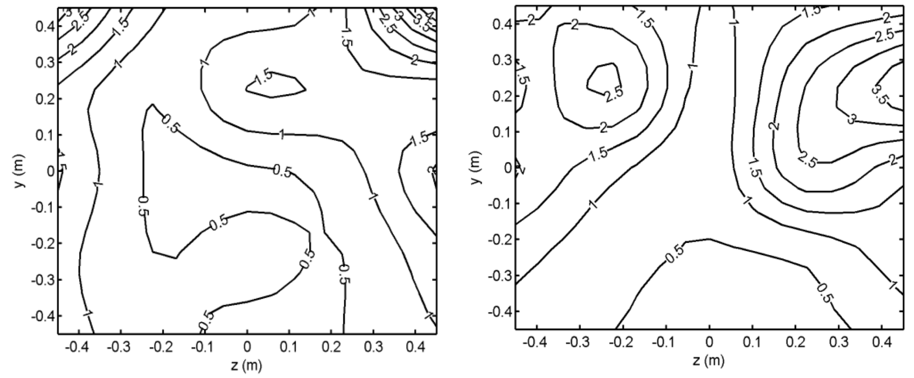

(a) α = 60° (b) α = 90°

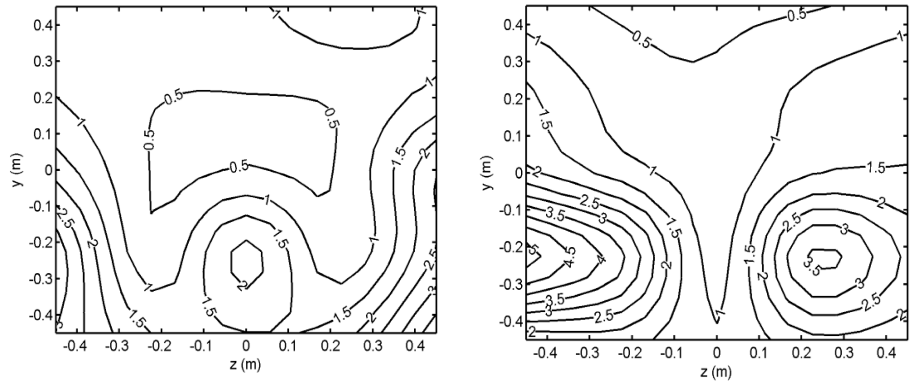

(c) α = 240° (d) α = 270°

Fig. 13 Value of $|R_\alpha|$ estimated for different angular positions during a characteristic cycle

relating to flow field surrounding the rotating test-sheet is required. At the time of undertaking the experiments it was not feasible to obtain this information. Thus there are a number of open questions. For example, to what extent are the characteristic signatures (explained above in terms of the rate of change) due to turbulence and what can be attributed solely to vortex shedding? While it is not possible to fully answer these questions given the experimental restrictions, it is worth considering the following hypothesis: coherent structures that can be identified in the flow field, which result from the auto-rotational motion of the test-sheet (e.g., vortices), are also identifiable in the pressure field. In order to prove or disprove this hypothesis and to provide an insight into the flow field, a CFD model has been developed and is outlined in the next section.

6. CFD model

The CFD modelling has the following two objectives for the present paper:

- to establish a general comparison with the experimental data in the time and frequency domains, and thus,
- to support, or reject, a potential relationship between the coherent structures identified in the pressure field and those in the flow field.

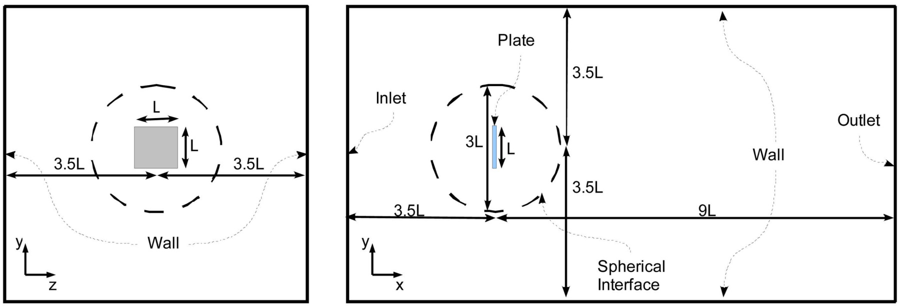

Fig. 14 3D computational boundaries and dimensions used in the CFD model

A computational fluid dynamics model of flat plate auto-rotation after Kakimpa *et al.* (2010a) has been used to simulate the unsteady-flow structures in the environment of the 1 m square plate, resembling that used in the experimental measurements. The plate was allowed to autorotate in a uniform, steady wind stream. Fig. 14 illustrates the 3D computational domain of dimensions 7 m × 7 m × 12.5 m. The plate and domain boundaries were modelled as walls with the no-slip condition applied, while the inlet was modelled as a constant velocity inflow boundary and the outlet as a constant pressure outflow boundary. Mean wind speeds of 5, 7.5, and 10 m/s were used for the fixed-axis auto-rotational simulations.

The domain was split into a spherical inner region that rotated monolithically with the plate in the auto-rotational simulation, and an outer region which remained stationary. The two regions were connected through a non-conformal sliding interface boundary. A quaternion based rigid body dynamics (RBD) model, described in Kakimpa *et al.* (2010b) was used to compute the rotational velocity of the inner region at each time step. The domain has been discretised using a structured hexahedral mesh of approximately 6 x 10^5 cells, with mesh refinement close to the plate boundary layer. The first layer of cells close to the plate has a cell spacing of approximately 0.01 m and a cell size growth ratio of approximately 1.2, away from the wall boundary. Grid sensitivity studies were carried out to ensure grid independence of the results.

Commercial CFD code ANYSYS FLUENT (Fluent Inc. 2006) was used to solve an arbitrary lagrangian-eulerian formulation of the 3D incompressible Navier-Stokes equations (Sarrate *et al.* 2001) by using a finite volume method. The realizable k-ε turbulence model (Shih *et al.* 1995) was used for turbulence modelling with an enhanced wall function. For the simulations presented in this paper, the inlet turbulence intensity and length scale were limited to 1% and 0.02 m, repectively, which corresponds to typical wind tunnel values (ESDU 1970). Second order upwind spatial discretization was used of the momentum, turbulent kinetic energy and turbulent dissipation rate with standard interpolation for the pressure variable. The SIMPLE algorithm was used for pressure-velocity coupling and second order implicit time-stepping scheme was used for the temporal discretisation.

6.1 Validation of CFD model in the frequency domain

The normalised spectra defined as nS_p / σ_p^2 (where n represents frequency; σ_p^2 is the variance of the process and the sub index p indicates pressure) of the data series at all sensor locations for U = 5, 7.5, and 10 m/s, was estimated using experimental and CFD data. The experimentally determined

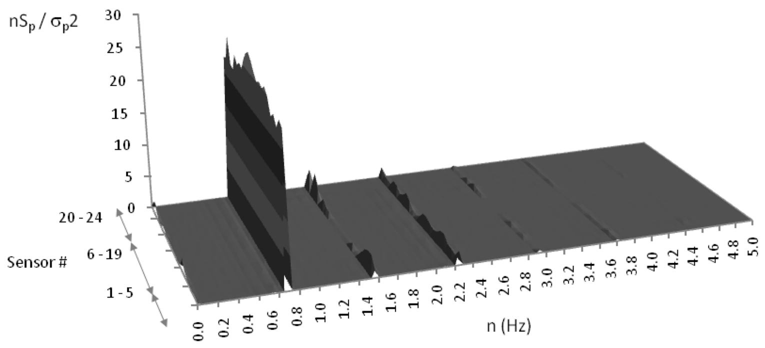

Fig. 15 Normalised spectra of experimental data for all sensors (#1 – #24), for U = 7.5 m/s

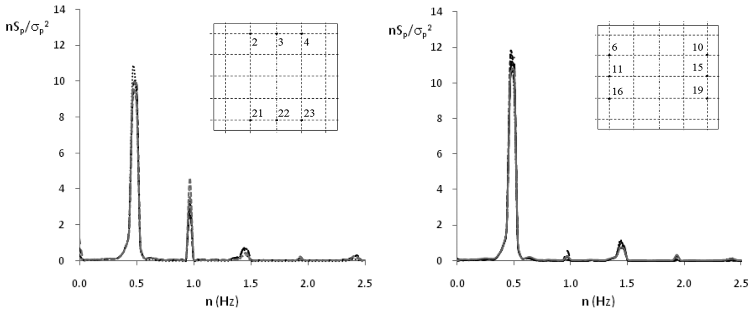

(a) Experimental

(b) Experimental

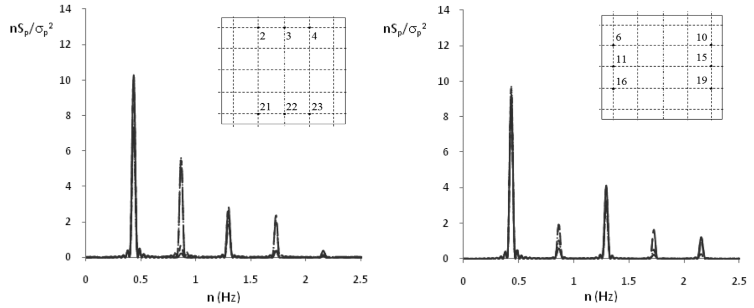

(a) CFD

(b) CFD

Fig. 16 Normalised spectra for sensors located at the centre of the top and bottom rows (a) and for sensors located at the sides (b), for U = 5 m/s

spectra for U = 7.5 m/s is shown in Fig. 15. It can be seen that, the main peak of the spectra corresponds to the fundamental frequency of rotation (n_0) which has been estimated as of 0.735 Hz. The patterns observed in this figure (e.g., the spatial distribution of peaks), are similar for the spectra estimated for U = 5 and 10 m/s whose values of n_0 were found to be 0.485 and 0.9 Hz respectively.

Fig. 15 shows that most of the energy quantified from the spectra appears to be contained in the first four peaks. According to the experimental data, these peaks concentrate at least 95 % of the total energy for U = 5, 7.5, and 10 m/s. It is also observed that the spectral ordinates from the first peak tend to increase in the region that is located around the geometrical centre of the test-sheet (sensor #13). In Fig. 16 the spectra computed for the experimental data are compared with those from the CFD data for $U = 5$ m/s.

Fig. 16 illustrate that the frequency associated with the higher-order peaks appears to be multiples of the fundamental frequency in both the experimental and CDF data. There are slight differences in the fundamental frequencies, which for the CFD case were estimated as of 0.43, 0.71 and 0.95 Hz for $U = 5$, 7.5, and 10 m/s, respectively. Thus, the difference with respect to the experimental data is of ~12.8 %, 3.5 %, and 5.5 % respectively. The total energy estimated to be contained in the first four peaks of the CFD spectra is of ~98%, i.e., 3% higher than its experimental equivalent. Although Fig. 16 show that the CFD spectral density appears to be distributed over a higher number of peaks, characteristic patterns observed in the experimental data seem to be reasonably well reproduced. For example, the relationship in amplitude between the second and third peaks in sensors located at the leading edges and sides which are shown in Fig. 16.

6.2 Validation of CFD model in the time domain

The average force coefficients per sensor that results from both the CFD and experimental data were compared. The surface pressures occurring on opposite faces of the CFD plate model were subtracted to define the net pressure which was then phase-averaged over a number of cycles to give the differential pressure signals equivalent to those presented in Fig. 3 for the experimental case. The values of C_{NP} were then compared as shown in Fig. 17 for a selected group of sensors, i.e., sensors #3 (upper row), #13 (geometrical centre), #18 (centre of second bottom row), and #23

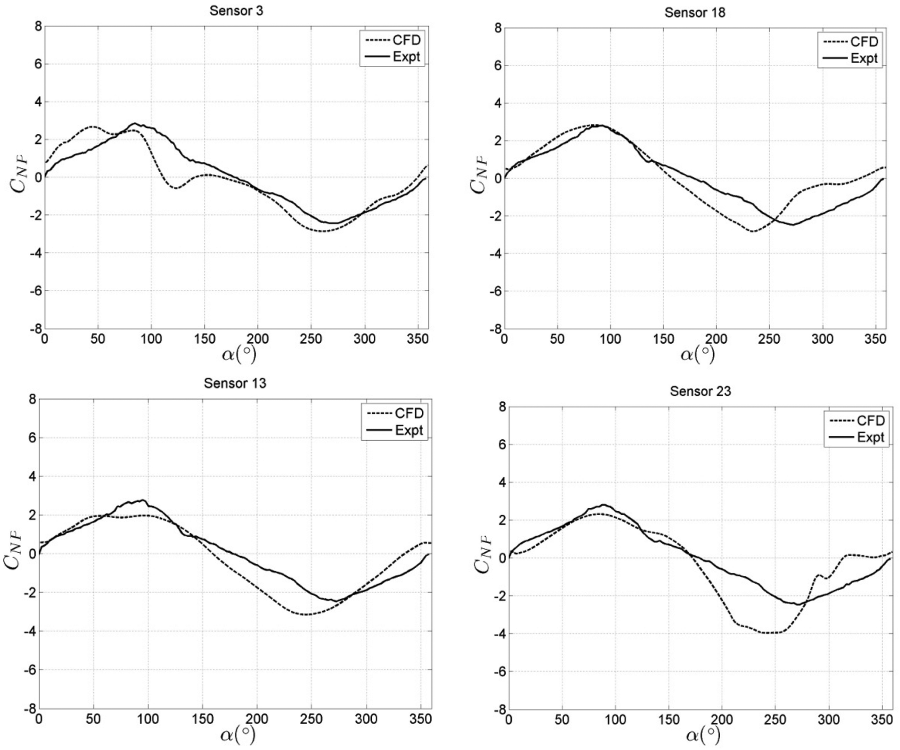

Fig. 17 Experimental and CFD phase-averaged differential pressure coefficients (C_{NP}) for various sensors obtained during the, $U = 5$ m/s test

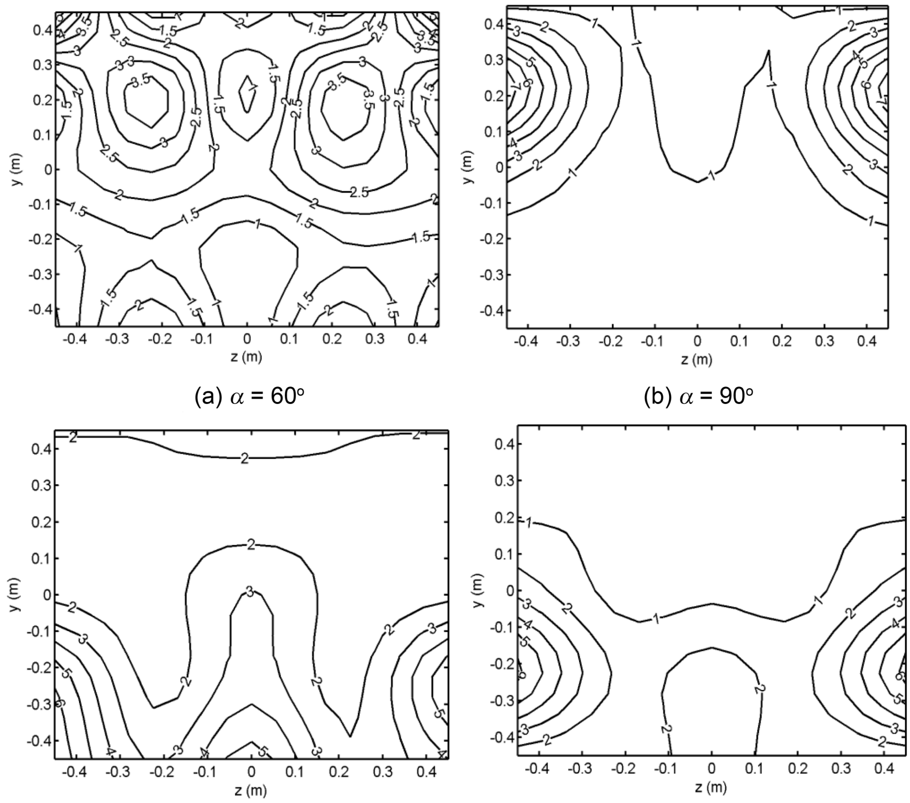

(a) α = 60° (b) α = 90°

(c) α = 240° (d) α = 270°

Fig. 18 Value of $|R_\alpha|$ estimated by using CFD data for different angular positions during a characteristic cycle, $U = 5$ m/s

(bottom row). Note that the data is being represented in angular (rather than in time) coordinates in order to be consistent with the presentation of force coefficients provided in previous sections.

It is observed in this figure that the overall peaks are located at slightly different values of the pitch angle (α), although the amplitude of the normal pressure coefficients is comparable. It is also noticeable that curves of C_{NP} inferred from the CFD model show some disturbances – see sensors #3 and #23, which would be equivalent to those presented in Figs. 5-7 for the experimental data. In the CFD model, such disturbances were observed at similar rates in each cycle for well defined angular intervals. The curves that correspond to the experimental case do not show such disturbances at the same rate because of the averaging process. Thus, in order to establish a qualitative comparison, the analysis of the rate of change presented in section 5 (experimental) was repeated using CFD data series. The result of this is shown in Fig. 18 in terms of $|R_\alpha|$, which can then be compared to those presented in Fig. 13.

Fig. 18 (CFD) shows similar patterns to Fig. 13 (experimental). That is, at α = 60°, the highest rate of change occurs in the region around the corners whereas at α = 90°, the peak rate of change is observed at the sides near the upper corners (with the highest values obtained from the CFD model). For α = 240°, coherent structures appear to concentrate at the bottom corners and at the centre, and at α = 270° peaks seem to occur at the bottom half, more clearly towards the sides.

These results seem to validate (for the current purposes) the CFD model. The evidence presented, indicate that coherent structures become more explicit at certain intervals within the auto-rotational domain, for example at angular ranges centred at α = 60°, 90°, 240°, and 270°. In the following section, it is shown that vortex shedding appears to occur at similar angular ranges. Although it is acknowledged that this simple fact does not prove a cause-effect relationship between the observed pressure disturbances and vortex shedding, it does not disprove the hypothesis.

7. Vortex shedding

In the past, auto-rotation of flat elements has been related to vortex shedding (Bustamante and Stone 1969, Smith 1970, Iversen 1979, Lugt 1983). For example, Bustamente and Stone (1970), Smith (1970), and Iversen (1979) suggested that autorotation of wings of symetrical cross section is due to a large vortex shed from the retreating face, whilst Lugt (1983) pointed out that the flow patterns are essentially independent of the Reynolds number (which seems to be supported by the experimental measurements presented in this paper). The CFD model discussed in the previous section, suggests that vortex shedding is present in the case study under discussion. This is shown in Figs. 19 and 20, where the 1 m square plate has been represented within the compuational environment at various angular positions during a cycle.

In Fig. 19, the vortex shedding appears to be locked to the frequency of rotation at the point of stable autorotation. The flow is characterized by a pronounced leading-edge vortex that forms and remains attached to the plate's retreating edge (upper edge) and is eventually shed into the wake. This attached vortex, which has been observed to create artificial lift during insect flight (Wang 2005) and in the auto-rotation of Maple seeds (Lentik *et al.* 2009), is attributed to the low pressure vortex core close to the plate that amplifies the differential pressures at the retreating edge of the plate. The advancing edge (lower edge) of the plate has shown weaker vortices that form due to stretching and roll-up of the vortex sheet at the trailing edge, and are quickly shed. The plate is observed to roll over the trailing edge vortex sheet, however due to the stronger influence of the stagnation pressure at the front, the effect of this on plate pressures appears to be negligible.

Fig. 20 illustrates the full three-dimensional flow structure behind the wake and shows that in addition to the leading edge vortex, two counter-rotating tip vortices of equal strength are also present in the flow. Tip vortices play a central role in delayed stall (compared to high aspect-ratio plates) by creating significant down-wash that supports the stable attachment of the leading edge vortex. A similar mechanism has been observed in low-aspect-ratio translating flat plates (Taira *et al.* 2009).

Through a complex interaction between the tip vortices with the leading edge vortices, the shedding of hairpin vortices is observed. These tip vortices are present at low angle of attack, and grow in strength as the angle of attack increases, contributing to the large differential pressures close to the side edges of the plate at higher angles of attack. Eventually, these tip vortices are shed into the wake as vortex tubes of significant helicity.

8. Conclusions

This investigation has described the distribution of pressures on different regions of an auto-

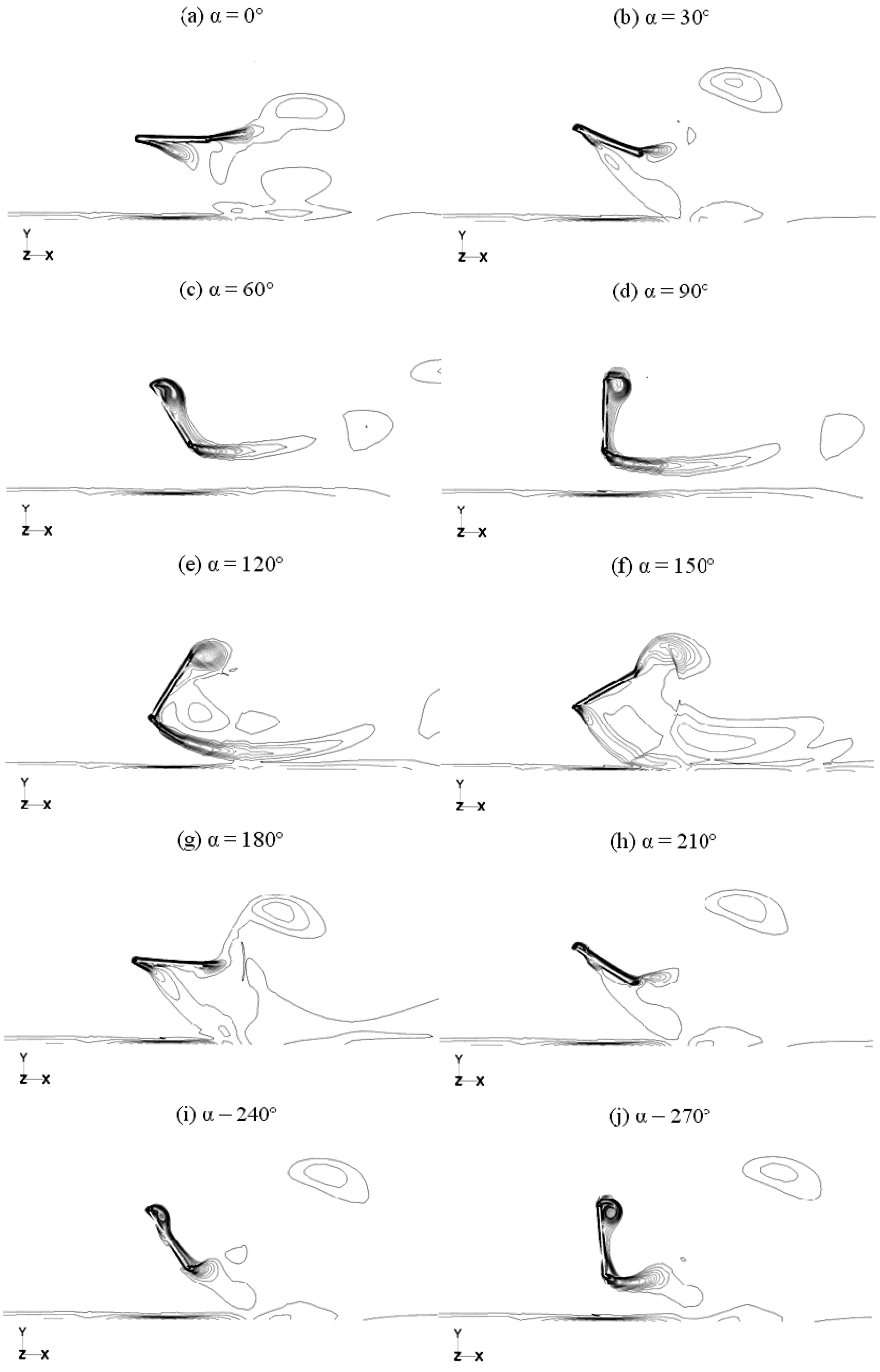
(a) α = 0°

(b) α = 30°

(c) α = 60°

(d) α = 90°

(e) α = 120°

(f) α = 150°

(g) α = 180°

(h) α = 210°

(i) α – 240°

(j) α – 270°

Fig. 19 Vorticity magnitude ($|\omega|$) contours from CFD results, showing vortex formation and shedding at the leading and trailing edges at different angles of attack during a rotational cycle

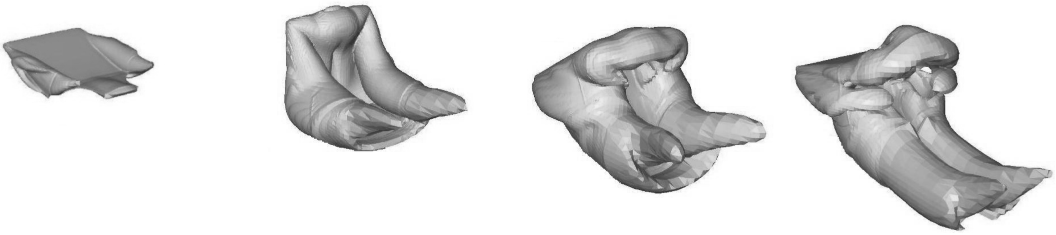

Fig. 20 Instantaneous iso-surfaces of vorticity magnitude ($|\omega|$) = 25 s^{-1} at; (a) $\alpha \approx 30^{\circ}$, (b) $\alpha \approx 90^{\circ}$, (c) $\alpha \approx 150^{\circ}$ and (d) $\alpha \approx 170^{\circ}$, showing the evolution of flow structures in the wake of an autorotating plate. Flow is mainly characterized by a leading edge vortex and two tip vortices that form and are shed into the wake during each cycle (Kakimpa *et al*. 2010c)

rotating plate. The non-averaged pressure field has shown asymmetries of the pressure distribution in the direction of auto-rotation which result in a net torque after each cycle that would contribute to stable autorotation. The lack of symmetry of the pressure configuration was also observed in the frequency domain via the corresponding power spectra. The spectral analysis showed regions located at the edges of the auto-rotating element which registered higher-order pressure components which were not observed (at least not at the same rate) at the centre of the plate. It was also noticeable that most of the energy was input to the plate at the frequency of auto-rotation. The relatively high values of the experimental force coefficients combined with a low index of variation (of about 2%) of subsequent peak pressures observed during stable autorotation suggested the occurrence of a lock-in effect in the experimental case study. This seemed to be confirmed by the CFD model where vortex shedding apparently locked-in to the rotational frequency was observed. On the other hand, the non-averaged pressure field also revealed the existence of unsteady pressure disturbances which concentrate at the edges of the auto-rotating plate. The analysis of those disturbances enabled coherent structures in the pressure field to be identified. Coherent structures would be characterised by a high speed of variation with respect to the pitch angle of the surface pressures located within a finite region, combined with a high local cross correlation of the pressure signal. The CFD simulation also reported pressure disturbances and coherent structures that are similar in location and extent to their experimental equivalent. The agreement between the CFD model and the experimental data enabled a cause-effect relationship between the coherent structures and vortex shedding to be suggested. That relationship requires further validation so that the energy transfer between the flow and the pressure field can be fully established, and each component (e.g., those induced by vorticity or turbulence) is specified in the time and frequency domains. Further research, involving combined plate pressure and wake flow measurements is thus recommended in order to validate the suggested relationship.

Acknowledgements

Funding for this research was provided by the United Kingdom's Engineering and Physical Sciences Research Council - grant number EP/F03489X/1. The authors also wish to express their gratitude to Mr. M. Vanderstam of the University of Birmingham for help with the construction of the experimental set.

References

Andronov, P.R., Grigorenko, D.A., Guvernyuk, S.V. and Dynnikova, G.Y. (2007), "Numerical simulation of plate autorotation in a viscous fluid flow", *J. Fluid Dynam.*, **42**(5), 719-731.

Baker, C.J. (2007), "The debris flight equations", *J. Wind Eng. Ind. Aerod.*, **95**(5), 329-353.

Cohen, M.J. (1976), "Aerodynamics of slender rolling wings at incidence in separated flow", *AIAA J.*, **14**, 886-893.

Bustamante, A.G. and Stone, G.W. (1969), "The autorotational characteristics of various shapes for subsonic and hypersonic flows", *AIAA J.*, **69**, 132.

Daniels, P. (1970), "A study of the nonlinear rolling motion of a four-finned missile", *J. Spacecraft Rockets*, **7**(5), 510-512.

Dong, H., Mittal, R. and Najjar, A.M. (2006), "Wake topology and hydrodynamic performance of low-aspect-ratio flapping foil", *J. Fluid Dynam.*, **566**, 309-343.

Dupleich, P. (1941), *Rotation in free fall of rectangular wings of elongated shape*, N.A.C.A., Tech Memo no. 1201.

ESDU International (1970), *Fluid forces and moments on flat plates*, Engineering Science Data Unit, Data Item 70015, ESDU International, London, U.K.. Fluent Inc. (2006), *ANSYS FLUENT 6.3 Documentation*

Glaser, J.C. and Northup, L.L. (1971), *Aerodynamic study of autorotating flat plates*, *Eng. Res. Inst.*, Iowa State Univ. Ames, Rep. ISU-ERI-Ames 71037.

Holmes, J.D. (1990), "Analysis and synthesis of pressure fluctuations on bluff bodies using eigenvectors", *J. Wind Eng. Ind. Aerod.*, **33**(1-2), 219-230.

Holmes, J.D. (2004), "Trajectories of spheres in strong winds with application to windborne debris", *J. Wind Eng. Ind. Aerod.*, **92**(1), 9-22.

Holmes, J.D., English, E. and Letchford, C. (2004), *Aerodynamic forces and moments on cubes and flat plates, with applications to wind-borne debris*, BBAA Conference, Ottawa.

Holmes, J.D., Letchford, C.W. and Lin, N. (2006), "Investigation of plate-type windborne debris - part II. computed trajectories", J. *Wind Eng. Ind. Aerod.*, **94**(2), 21-39.

Iversen, J.D. (1979), "Autorotating flat-plate wings: the effect of the moment of inertia, geometry and Reynolds number", *J.Fluid Mech.*, **92**(2), 327-348.

Kakimpa, B., Hargreaves, D.M., Owen, J.S., Martinez-Vazquez, P., Baker, C.J., Sterling, M. and Quinn, A.D. (2010a), "CFD modelling of free-flight and auto-rotation of plate type debris", *Wind Struct.*, **13**(2), 169-189.

Kakimpa, B., Hargreaves, D.M. and Owen, J.S. (2010b), "Aerodynamic characterization of static and autorotating plates using coupled CFD-RBD simulations", *Proceedings of the the 5th International Symposium on Computational Wind Engineering*, Chapel Hill, North Carolina, USA, May.

Kakimpa, B., Hargreaves, D. and Owen, J. (2010c), "A singularity-free model for 3D windborne debris flight", *Proceedings of the 9th UK Conference on Wind Engineering*, University of Bristol, Sept.

Kordi, B., Traczuk, G. and Kopp, G. (2010), "Effects of wind direction on the flight trajectories of roof sheathing panels under high winds", *Wind Struct.*, **13**(2), 145 -167.

Lentink, D., Dickson, W.B., van Leeuwen, J.L. and Dickinson, M.H. (2009), "Leading-edge vortices elevate lift of autorotating plant seeds", *Science*, **324**(5933), 1438-1440.

Lugt, H.J. (1980), "Autorotation of an elliptic cylinder about an axis perpendicular to the flow", *J. Fluid Mech.*, **99**(4), 817-840

Lugt, H.J. (1983), "Autorotation", *Annu. Rev. Fluid Mech.*, **15**, 123-147.

Martinez-Vazquez, P., Baker ,C.J., Sterling, M., Quinn, A.D. and Richards, P.J. (2009), "Aerodynamic forces on fixed and rotating plates", *Wind Struct.*, **13**(2), 127-144.

Martinez-Vazquez, P., Sterling, M., Baker, C.J., Quinn, A.D. and Richards, P.J. (2010), "Autorotation of square plates, with application to windborne debris", *Wind Struct.*, **14**(2), 167-186.

Mittal, R., Seshadri, V. and Udaykumar, H.S. (2004), "Flutter, tumble and vortex induced autorotation", *J. Theor. Comput. Fluid Dynam.*, **17**(3), 165-170.

Newmark, S. (1963), "Rotating aerofoils and flaps", *T. Jpn.Soc. R. Aeronaut. S.*, **67**, 47-63.

Riabouchinsky, D.P. (1935), "Thirty years of theoretical and experimental research in Fluid Mechanics", *T. Jpn.Soc. R. Aeronaut. S.*, **39**, 282-348.

Richards, P.J., Williams, N., Laing, B., McCarty, M. and Pond, M. (2008), "Numerical calculation of the 3-dimensional motion of wind-borne debris", *J. Wind Eng. Ind. Aerod.*, **96**, 2188-2202.

Smith, E.H. (1971), *Autorotating wings: an experimental investigation*, Univ. Michigan Aerospace Eng. Rep. 01954-2-7.

Sarrate, J., Huerta, A. and Donea, J, (2001), “Arbitrary lagrangian-eulerian formulation for fluid-rigid body interaction”, *Comput. Method. Appl. M.*,**190**(24-25), 3171-3188.

Shih, T.H., Liou, W.W., Shabbir, A., Yang, Z. and Zhu, J. (1995), “A new k-å eddy-viscosity model for high Reynolds number turbulent flows - model development and validation”, *Comput. Fluids*, **24**(3), 227-238.

Tachikawa, M. (1983), “Trajectories of flat plates in uniform flow with application to wind-generated missiles”, *J. Wind Eng. Ind. Aerod.*, **14**(1-3), 443-453.

Taira, K. and Colonius, T. (2009), “Three-dimensional flows around low-aspect-ratio flat-plate wings at low Reynolds numbers”, *J. Fluid Mech*,, **623**, 187-207

Wang, Z.J. (2005), “Dissecting insect flight”, *Annu. Rev. Fluid Mech.*, **37**, 183-210.

Wang, K.J. and Letchford, C.W. (2003), “Flight debris behaviour”, Proceeedings *of the 11th International Conference on Wind Engineering.*

Wills, J.A.B., Lee, B.E. and Wyatt, T.A. (2002), “A model of wind-borne debris damage”, *J. Wind Eng. Ind. Aerod.*, **90**(4-5), 555-565.

JH